Observation of tropical cyclones by high-resolution scatterometry

Y. Quilfen, B. Chapron, T. Elfouhaily, K. Katsaros,[1] and J. Tournadre

Laboratoire d'Océanographie Spatiale, Institut Français de Recherche pour l'Exploitation de la Mer
Plouzané, France

Abstract. Unprecedented views of surface wind fields in tropical cyclones (hereafter TCs) are provided by the European Remote Sensing Satellite (ERS) C band scatterometer. Scatterometer measurements at C band are able to penetrate convective storms clouds, observing the surface wind fields with good accuracy. However the resolution of the measurements (50×50 km^2) limits the interpretation of the scatterometer signals in such mesoscale events. The strong gradients of the surface wind existing at scales of a few kms are smoothed in the measured features such as the intensity and location of the wind maxima, and the position of the center. Beyond the ERS systems, the scatterometers on-board the ADEOS and METOP satellites, designed by the Jet Propulsion Laboratory and by the European Space Agency, respectively, will be able to produce measurements of the backscattering coefficient at about 25×25 km^2 resolution. A few sets of ERS-1 orbits sampling TC events were produced with an experimental 25×25 km^2 resolution. Enhancing the resolution by a factor of 2 allows location of the wind maxima and minima in a TC with a much better accuracy than at 50 km resolution. In addition, a better resolution reduces the geophysical noise (variability of wind speed within the cell and effect of rain) that dominates the radiometric noise and hence improves the definition of the backscattering measurements. A comprehensive analysis of the backscattering measurements in the case of high winds and high sea states obtained within TCs is proposed in order to refine the interpretation of the wind vector derived from a backscattering model that is currently only calibrated up to moderate winds (< 20 m/s) in neutral conditions. Observations of the TOPEX-POSEIDON dual-frequency altimeter are also used for that purpose. Patterns of the surface winds in TCs are described and characteristic features concerning asymmetries in the maximum winds and in the divergence field are discussed.

1. Introduction

The surface wind field is one of the most important parameters for estimating the surface heat fluxes that drive the tropical cyclones (TCs) [*Emanuel*, 1988]. Surface data are very scarce, and satellite-borne radiometers in visible and infrared channels are limited to observing the upper regions of the storms due to the widespread cloud cover. These data are currently the primary source for inferring the maximum surface wind speed in TC forecast centers around the world [*Dvorak*, 1976]. The polar orbiting European Remote-Sensing Satellites (ERS-1 and ERS-2), launched by the European Space Agency (ESA) on July 17, 1991, and April 21, 1995, respectively, carry the C band active microwave instrument (AMI). The AMI is operated as a synthetic aperture radar for surface imaging and as a scatterometer to

measure the surface wind vector with a nominal resolution of 50×50 km^2. A limited data set of experimental products were also generated by the french space agency (Centre National d'Etudes Spatiales) with a resolution of 25×25 km^2 to investigate its feasibility and its interest for mesoscale meteorology. Both wind speed and direction can be retrieved by inverting an empirical model relating the radar backscatter signals to the 10 m neutral wind vector. The model validity has been verified in a statistical sense [*Quilfen and Bentamy*, 1994; *Graber et al.*, 1996], but very little is known about the scatterometer signals in TCs, where very high winds and sea states are encountered. A TC case has been selected to illustrate the potentialities of the scatterometer measurements and the advantages of the higher resolution. This case study outlines the great improvement to be expected in TC analysis and forecasting with future scatterometers. Moreover, it shows the need to further analyze the microwave signature in these extreme events, the scatterometer wind speed being underestimated as it was found to be with data from the Seasat scatterometer [*Jones et al*, 1982]. Furthermore, the heavy rains occurring in TCs are likely to influence the signals at C band. To verify the scatterometer inferred winds in TCs, other microwave data sources providing environmental parameters are used. The

[1]Now at Atlantic Oceanographic and Meteorological Laboratory, National Oceanic and Atmospheric Administration, Miami, Florida.
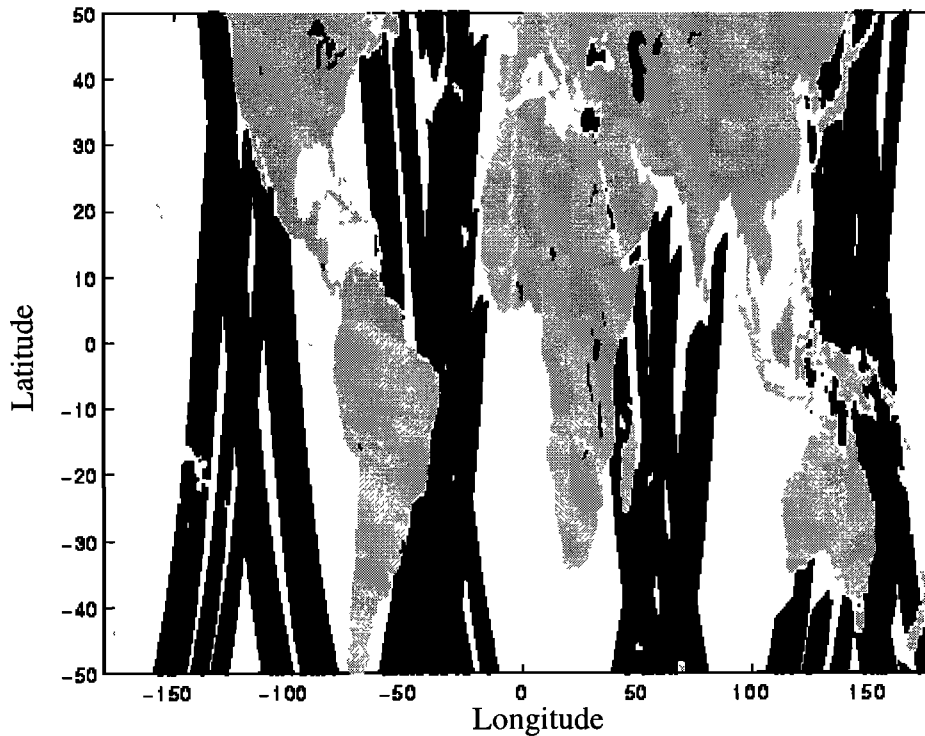
Figure 1. ERS-1 scatterometer coverage for the 29 orbits processed in the HR mode.

altimeter on board the TOPEX-POSEIDON satellite (hereafter T/P) provides high resolution measurements of the wind speed and sea state and can be used to provide an estimate of the rain events [*Tournadre and Morland*, 1997]. Surface wind and wave parameters at various scales will thus help to better describe the wind and wave patterns within TCs as well as to study the associated air-sea interaction mechanisms. However, altimeters only sample a narrow swath at nadir. The two DMSP satellites F11 and F12 carrying the special sensor microwave imager (SSM/I) overlap with ERS and provide a unique opportunity to relate convective patterns of clouds and precipitation to surface winds within TCs. The SSM/I instruments have a broad swath of 1400 km width and are in a highly inclined Sun-synchronous orbit with local overpass times near dawn and dusk. The resolution of the SSM/I varies from 15 to 50 km as frequency varies from 85 to 19 GHZ.

Section 2 presents the data. Section 3 is devoted to a comparative analysis of the normalized radar cross sections (NRCS) for the high-resolution and low-resolution modes of the scatterometer. It shows that measurements at high resolution lead to a better evaluation of the radar measurements in cases of high wind gradients. Improved estimates of maximum wind radii and storm-surge forecasting may then be expected for operational purposes. Section 4 is dedicated to the investigation of the backscattering signal for high wind and sea state conditions as measured by the different microwave instruments. Section 5 describes the wind patterns and their evolution for TC Elsie, a western Pacific typhoon that was well sampled by the ERS-1 scatterometer.

2. Data

The ERS scatterometers use three antennae pointing in azimuts of 45°, 90° and 135° with respect to the satellite ground track. It obtains thus for each node three independent measurements of the NRCS. Each antenna illuminates a 500-km-wide swath, covering a range of incidence angles from 18° to 60°.

ERS-1 scatterometer data used to compute winds are the NRCS (σ_0) provided by the Centre National d'Etudes Spatiales [*Malardé*, 1992]. Twenty-nine orbits covering TCs occurring between July 1992 and November 1992 were processed. The data coverage is shown in Figure 1. Two grids are available for the NRCS measurements sampled over the 500-km-wide swath: a 25 km grid for the 50 km low-resolution mode (LR) and a 12.5 km grid for the 25 km high-resolution mode (HR). For each node a noise estimation from two parameters, the radiometric resolution Kp and the NRCS standard deviation STD, can be associated with each of the three antennae measurements.

The Kp is the classical parameter used to characterize the noise. It is defined as the standard deviation of the raw NRCS measurements used to evaluate the mean NRCS value characterizing the target over a given area [*Fischer*, 1972]. The theoretical developments presented by *Fisher* [1972] lead to the following formulation for Kp:

$$K_p = \left[\frac{1}{N} \times \left(1 + \frac{2}{\text{SNR}} + \frac{1}{\text{SNR}^2} \times \left(1 + \frac{T_{sn}}{T_N} \right) \right) \right]^{1/2} \tag{1}$$

where N is the number of independent measurements used to estimate the NRCS (about 300 for the HR and 1200 for the LR), SNR is the signal to noise ratio, T_{s_n} is the signal integration time and T_N is the noise integration time.

As this computation makes some assumption about the target characteristics, one being its stationarity, we also use another parameter to characterize the noise, STD , defined as

$$\text{STD} = \left[\frac{1}{N} \times \sum_{i=1}^{N} \left(\sigma_{0i}^2 - \sigma_0^2\right)\right]^{1/2} / \sigma_0 \qquad (2)$$

where N is the number of independent measurements (σ_{0i}) used to estimate the mean NRCS (σ_0).

The NRCS produced by the CNES were calibrated and validated against those delivered by ESA, showing the consistency of the two NRCS sources [Malardé, 1992].

To compute the wind vector, NRCS data were processed using the C band model described below (referenced as CMOD_IFR2) and with the algorithms described by Quilfen and Bentamy [1994]. Following Long [1992], the C band model is expressed as

$$\sigma_0 = b_0(1 + b_1 \times \cos\emptyset + b_2 \times \cos2\emptyset) \qquad (3)$$

where $b_0 = 10^{a + b\sqrt{V}}$ $\emptyset = \Phi - \Psi$

a and b are arrangements of polynomials of order up to 3 in θ, and b_1 and b_2 are arrangements of polynomials of order up to 2 in θ and V; θ is the incidence angle, V is the wind speed, Φ is the wind direction, and Ψ is the antenna azimuth angle. The model is fully described in appendix.

Parameters a, b, b_1, and b_2 were calibrated with a method minimizing a maximum likelihood estimator between the σ_0 measured values and the C band model values [Bentamy et al., 1994]. Data from the U.S. National Oceanic and Atmospheric Administration (NOAA), collected by 24 buoys considered to be moored far enough from the shore during the time period March-June 1992, were used to calibrate a and b. Selected data from the European Centre for Medium-Range Weather Forecasts (ECMWF) wind analysis were used to calibrate b_1 and b_2 [Quilfen and Bentamy, 1994]. As there were not enough reference data of high wind speed to define and to calibrate the C band model shape for these conditions, a mean wind speed dependent bias was estimated and is used to correct the wind speed computed by the model inversion process beyond 10 m/s. Indeed, the calibration process is a global one-step process and would have required many high-wind measurements to converge, while much less measurements are required to estimate a bias correction. An extended buoy data set was used to estimate this bias correction (March 1992 to October 1993). The bias correction is described in the appendix and its adequacy is discussed in section 4.

For the validation, another extended NOAA buoy data set is used for the time period July 1992 to February 1994. It is independent of the one used to calibrate the C band model, with the exception of the high winds used to estimate the bias term between March 1992 to October 1993.

We also use in this study one track of the T/P altimeter delivered by the Archiving, Validation, and Interpretation of Satellite Data in Oceanography (AVISO) processing center [AVISO, 1992]. This track intersects TC Elsie close to its center on November 4, 1992.

In order to identify convective regions, the Petty and Katsaros [1990] algorithms have been used to infer the following parameters from SSM/I brightness temperature data on board the F11 DMSP satellite: the integrated atmospheric water vapor, the integrated cloud liquid water, and an index of scattering by large ice particles (based on a combination of brightness temperatures at 85 GHz). Large values of the latter parameter are indicative of convection.

3. Comparison of the NRCS Distributions for the High- and Low-Resolution Data

3.1. Characterization of the Noise

The accuracy of NRCS measurements is generally defined in terms of radiometric resolution Kp (defined in section 2). Kp provides an estimation of the noise contribution from the receiver and due to the speckle (the random nature of the target). This calculation relies on the basic assumption of stationarity of the target, which is not always true, as is outlined below.

In comparing the noise for the HR and LR measurements, we are also interested in the non stationarity of the target. For this purpose, a measure of the NRCS standard deviation (STD) defined in section 2 is performed for each NRCS measurement, in addition to the Kp estimation, which is a more theoretical and statistical estimation of the noise. Non stationary effects are mainly due to the mesoscale geophysical variability (a few kms to a few hundred kms in scale), which is of great interest for the dynamics of the atmosphere. In particular, it will be shown that the mesoscale wind patterns are better captured with the HR measurements.

Figure 2 shows the mean values of the NRCS, the radiometric resolution Kp and the standard deviation STD, for the LR and HR respectively, over the 29 orbits (about 300,000 measurements, land points being discarded by using the same mask for the two resolutions). Data collected to compute the distributions are sampled every 50 km. The differences between the mean NRCS for the HR and LR never exceed 0.15 dB, which is under the noise level of about 0.3 dB. Averaging the NRCS over different cell sizes does not introduce any significant bias (at the 95% confidence level, not shown).

The mean Kp varies from 2.8% to 4% for the LR and from 5.5% to 7.2% for the HR. Values of Kp for the HR re-
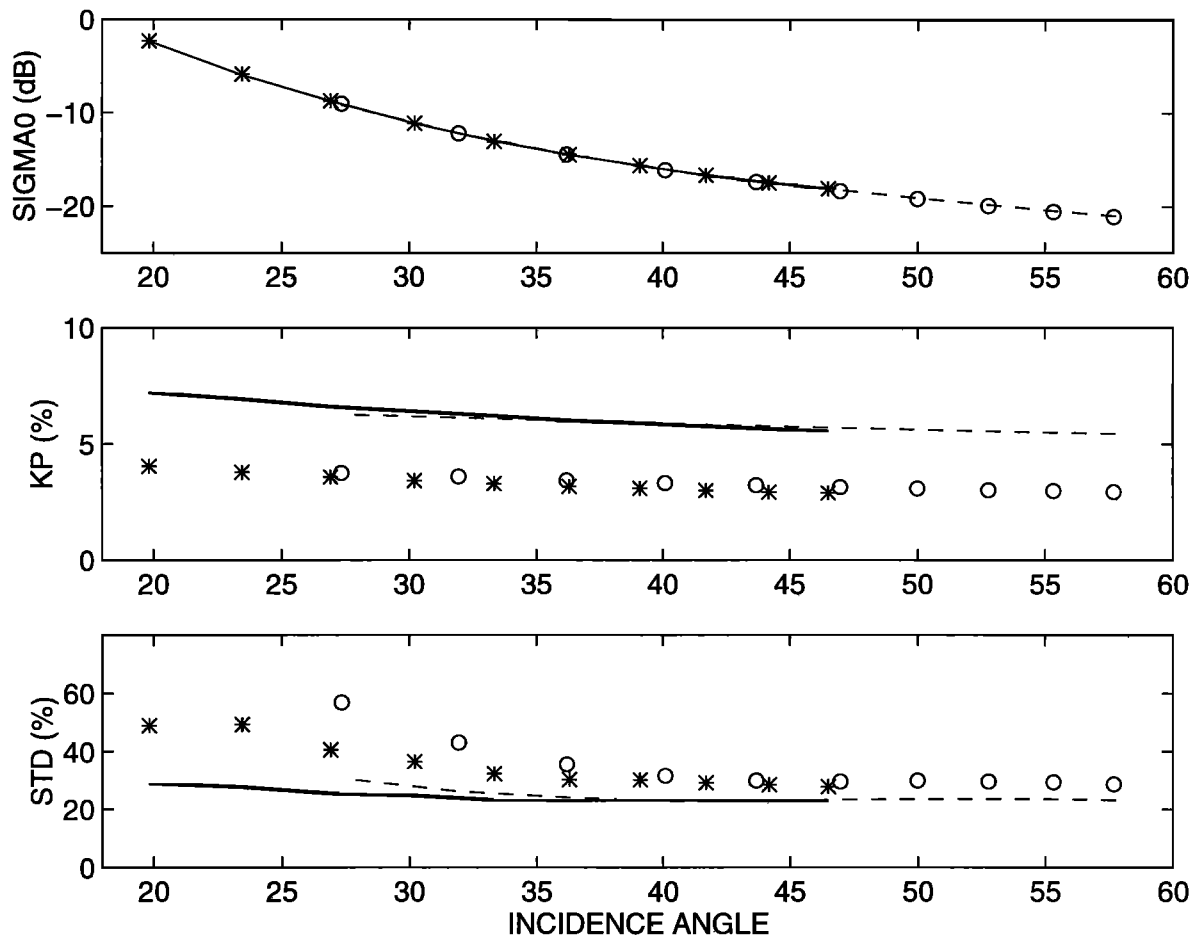
Figure 2. Mean values as a function of the incidence angle (in degrees): (top) NRCS σ_0 in decibels, (middle) radiometric resolution Kp in percentage, and (bottom) NRCS standard deviations STD in percentage. Solid and dashed lines are for the HR measurements of the central and lateral antennae, respectively; stars and open circles are for the LR measurements of the central and lateral antennae, respectively.

main lower than the ESA initial specifications (of the order of 8%). As the Kp depends upon the signal to noise ratio, it depends on the incidence angle but also on the wind conditions. It is higher for low wind speeds and for cross-wind measurements. It is rather difficult to compare the LR and HR measurements in terms of the accuracy of the estimated NRCS because the computed Kp includes only a part of the total noise, i.e., the receiver thermal noise and the speckle.

The STDs also include the geophysical effects, mainly due to the presence of wind gradients or to attenuation variations due to rain, and the variability due to the NRCS cross-track gradients. The gradient being higher at low incidence angles, the mean STDs are also higher. Thus both effects, the geophysical variability that is reduced for the HR and the NRCS cross-track gradients, can explain why the mean STDs are higher for the LR although the Kp are lower.

In order to better characterize the NRCS noise, the distribution of STDs over the 29 orbits was computed and is displayed in Figures 3a and 3b for incidence angles of 27° and 57°, respectively. As was noted above, it appears that the mean STDs are higher for the LR, mainly on account of the cross-track NRCS gradient. The most interesting feature is

that the dispersion is much lower for the HR, meaning that the non stationary part of the target, i.e., the geophysical effects (wind and sea state variability within the cell or rain effects), is greatly reduced. The NRCS estimation is thus improved in many cases.

3.2. Example of a Geophysical Phenomenon

Figure 4 gives a typical example summarizing the features discussed above. It shows the NRCS standard deviations for the case of TC Elsie (November 3, 1992) which will be analyzed in more detail in the following sections. There is much more structure in the LR measurement noise (Figure 4b), while STDs are more uniform for the HR mode (Figure 4c). STDs are much higher for the low incidence angles of the LR measurements, while this effect is much reduced in the case of the HR. Moreover, non stationary effects in the 50 km cells due to the geophysical variability are clearly highlighted in the area near 12°N, 142°E. This region corresponds to high incidence angle and high wind measurements. As shown in the wind field (Figure 4a), strong gradients occur with low level convergence of the flow in the western eyewall of the TC. The maximum STDs
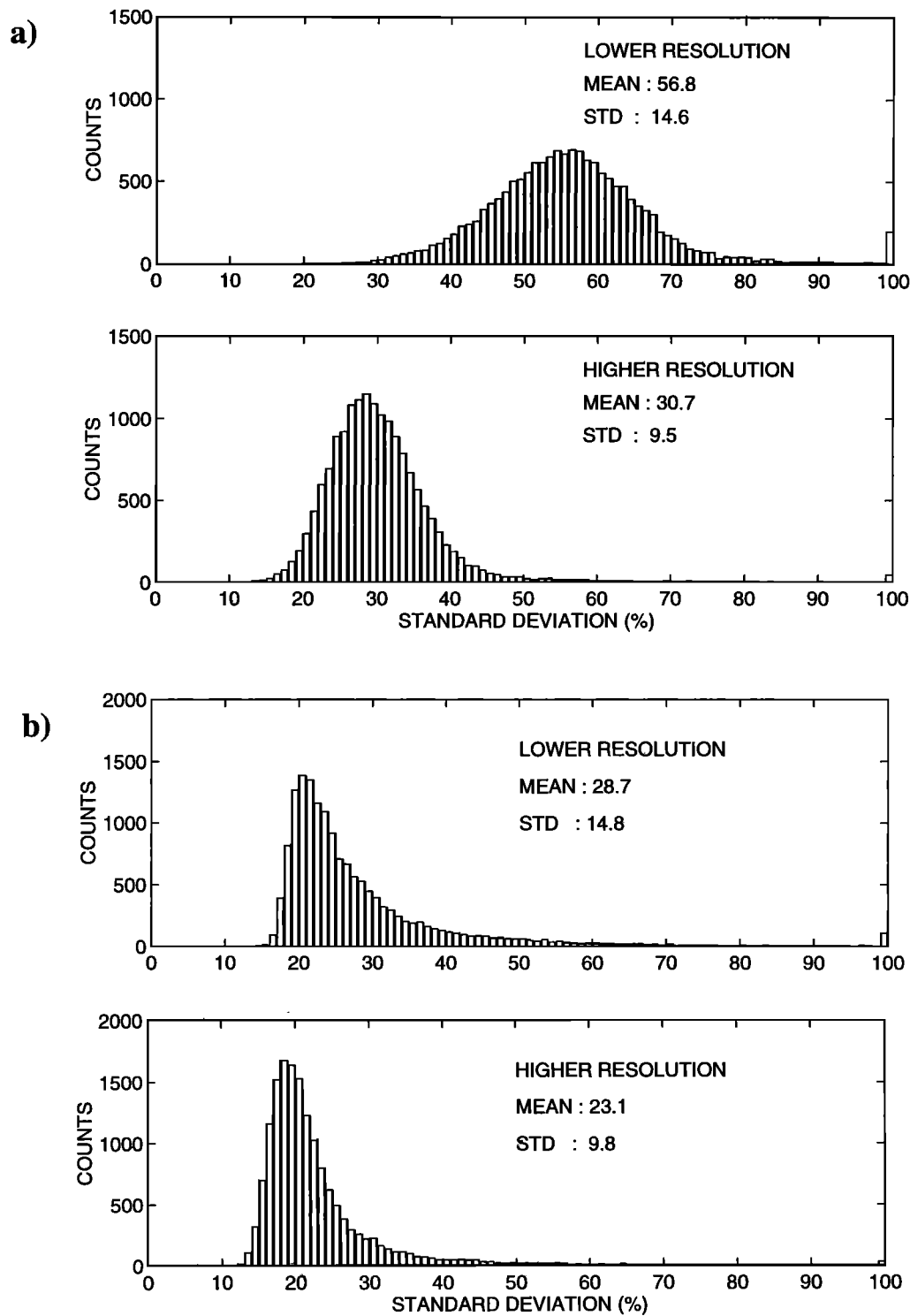
Figure 3. Distribution of the NRCS standard deviations (in percentage) for the HR and LR NRCS measurements for incidence angles of (a) 27° and (b) 57°.

in this area are of the order of 50% for the LR measurements and of the order of 30% for the HR measurements. Such a result is much closer to the mean value of 23% (Figure 3b), which confirms that the HR measurements may provide a better estimate of the NRCS field and thus a better representation of the wind structures.

Another maximum of STD occurs in the area centered on the island of Guam (approximately 145°E, 13.4°N). The mean level of the backscattered signal is different for the sea and for the land. This discontinuity is characterized by high STDs values.

It appears that the ERS scatterometer high resolution does not deteriorate the radar cross-section measurement. Further, it reduces the non stationary part of the wind variability within the cell to improve the definition of the wind structures.
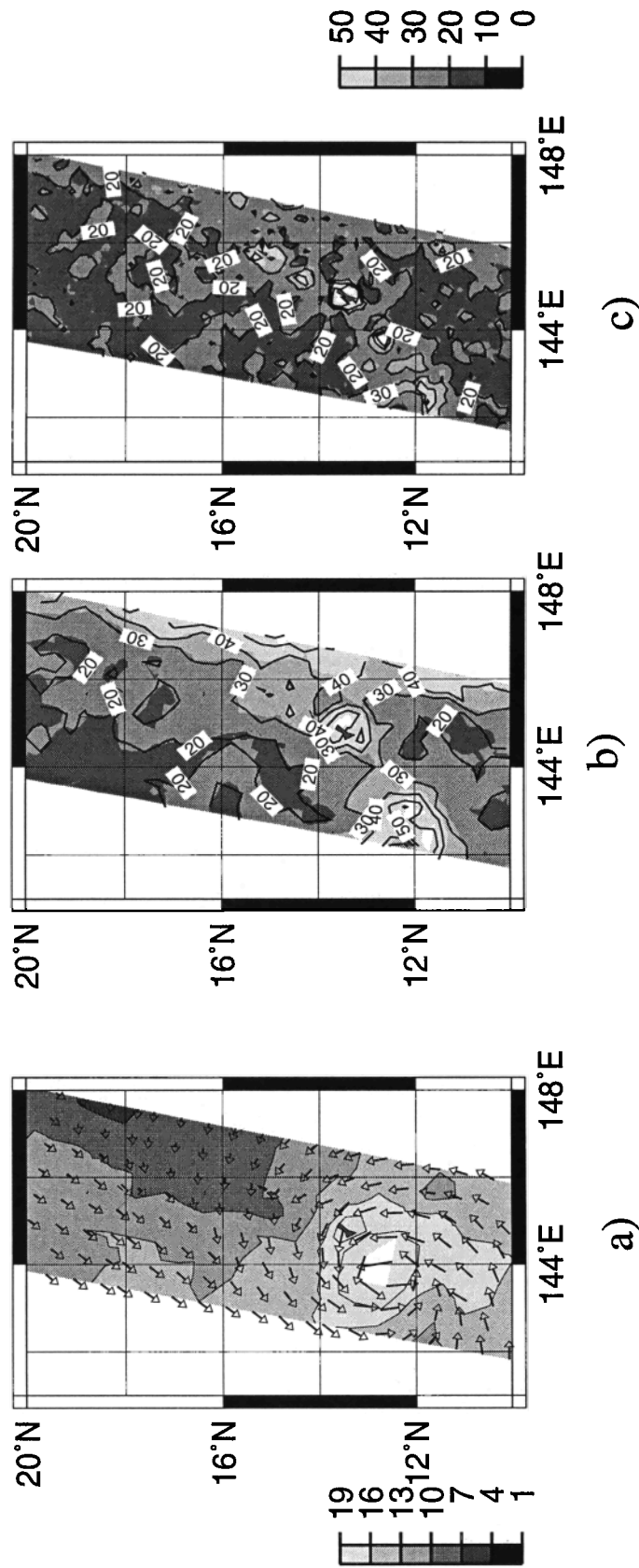
Figure 4. (a) Surface wind field (left scale in m/s); (b) LR NRCS standard deviations; (c) HR NRCS standard deviations (right scale in percentage). Case of tropical cyclone Elsie (November, 3, 1992).
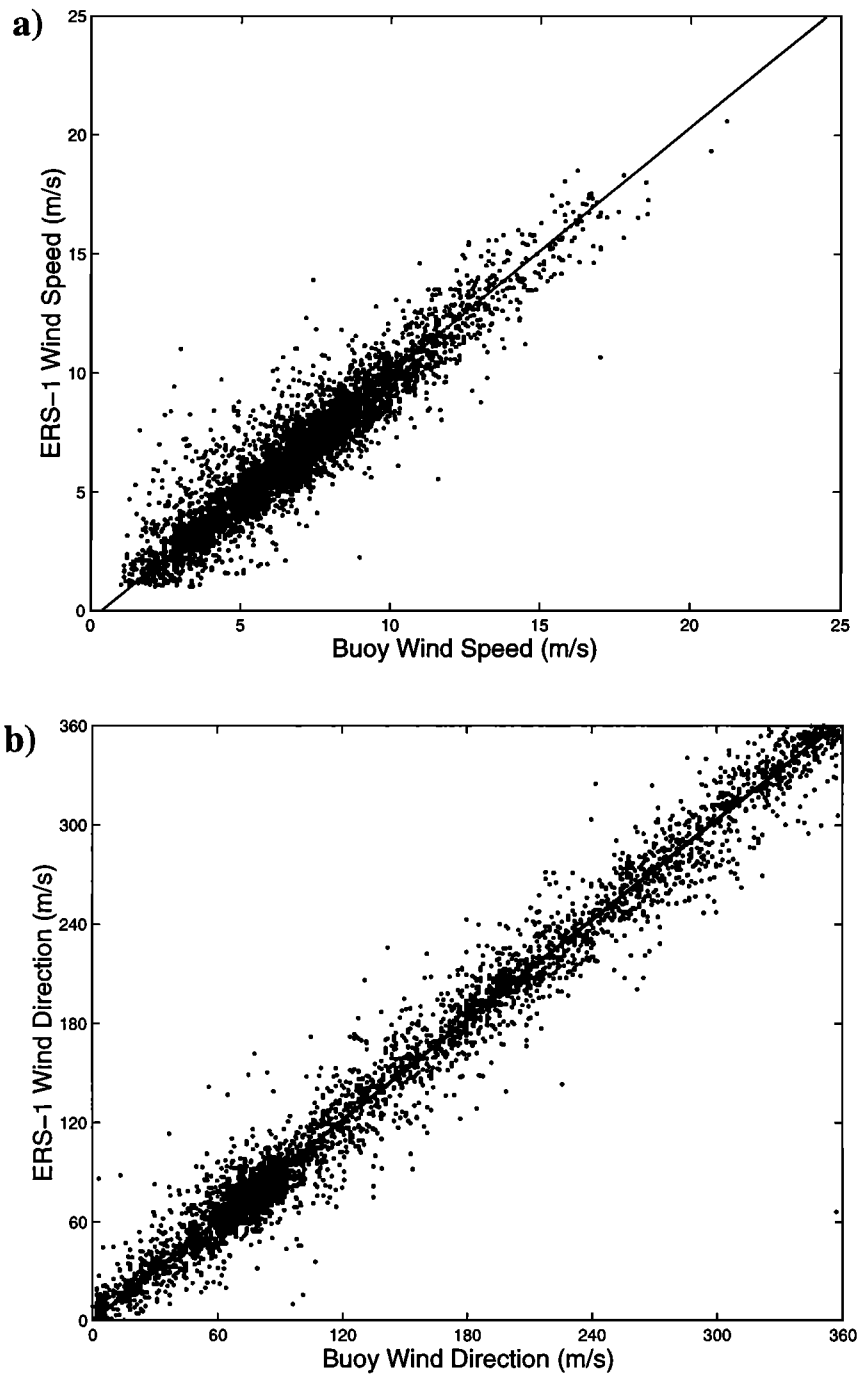
Figure 5. Comparison of (a) the wind speeds (m/s), and (b) the wind directions (degrees) observed by the ERS-1 scatterometer with those measured by the NOAA buoys. The symmetrical regression lines are shown.

4. The Microwave Signature at High Wind Speeds

4.1. Evaluation of the C Band Model

High wind speed (above 15 m/s) measurements at the sea surface by means of anemometers are very scarce, and their accuracy is being questioned for high sea-state conditions because of the buoy movements and the anemometers being shadowed by the waves [*Large et al.*,1995]. For this reason and also because storms are often inaccurately represented in the numerical weather prediction models at the scale of the scatterometer footprint, there is no good reference high-wind data set, except for airborne flight level measurements in atlantic hurricanes, against which microwave measurements may be calibrated. Consequently, the scatterometer C band model CMOD_IFR2 uses very few high-wind measurements, and the model shape for high winds (above 15 m/s) must be considered as an extrapolation of the shape for moderate to high winds. Since predicted NRCS values were

found to increase too fast with the wind speed [*Bentamy et al.*, 1994], high wind speed is likely to be underestimated. Thus a bias correction of the scatterometer winds has been estimated (see appendix) and is applied to better estimate high winds. Scatterometer winds at 50 km resolution have then been validated against other data sources and intensively compared with collocated measurements (within 25 km and 10 mn) of the NOAA buoys. Buoy measurements are converted to 10 m neutral winds. Between July 1992 and February 1994, 3433 collocated pairs were thus available to perform such comparisons. For each ERS-1 cell the wind vector considered, among the four possible solutions, is the one whose direction is the closest to the buoy wind direction [*Quilfen and Bentamy*, 1994]. Figures 5a and 5b show an overall reasonable agreement, also shown by *Graber et al.*, [1996]. A symmetrical regression is performed to take into account the fact that each data set has its own intrinsic errors, the regression coefficients thus being invariant with respect to the interchange of buoy and scatterometer data. The mean biases are negligible at a significance level of 95%. The-root-mean-square (rms) errors are 1.38 m/s and 18.6° for the wind speed and direction, respectively. Correlation coefficients between buoy and ERS-1 winds are 0.91 and 0.98 for speed and direction, respectively. The symmetrical regression coefficients are 1.04 and 1.01 for speed and direction, respectively. However, as was mentioned above, the bias is likely to be wind speed dependent, and although a bias correction is applied, differences are still significant for winds greater than 15 m/s [*Graber et al.*, 1996]. It must be noted that these biases are difficult to quantify because the high-wind buoy measurements are also of lower accuracy and because of their large temporal and spatial variability. Graber et al. also showed that at high winds the estimated bias is even greater for the ESA model function CMOD4 [*Stoffelen and Anderson*, 1997], while it is close to 0 for the model function developed by the Jet Propulsion Laboratory [*Freilich and Dunbar*, 1993]. The latter model is defined with a tabulated model function and will not depend on a mathematical expression. It can then be hypothesized that biases at high winds in CMOD4 and CMOD_IFR2 are related to an improper extrapolation by both models: the NRCS square root dependency as a function of the wind speed or the model coefficients do not seem to hold at high wind speed (above 15 m/s).

To better illustrate such a conclusion, the measured and predicted by CMOD_IFR2 NRCS have been compared

Figure 6. (a) Dependence of the term b_0 on the wind speed (m/s) as provided by CMOD_IFR2 (dashed line) and as estimated from measured NRCS (solid line). (b) Dependence of the term b_1 on the wind speed (m/s), (top) as provided by CMOD_IFR2 and (bottom) as estimated from measured NRCS. (c) Dependence of the term b_2 on the wind speed (m/s), (top) as provided by CMOD_IFR2 and (bottom) as estimated from measured NRCS. Computations are done for 25° (curve 1), 35° (curve 2), 45° (curve 3), and 55° (curve 4) of incidence angle.

(Figure 6). Six weeks of scatterometer measurements collocated with the ECMWF analyses have been considered because there are not enough buoy data to do this analysis. For each week the model parameters b_0, b_1, and b_2 (see section 2) have been estimated. Mean values and standard

deviations are then compared with the CMOD_IFR2 values. Computations are made as follows:

$$b_0 = (S_u + S_d + 2xS_c)/4$$

$$b_1 = (S_u - S_d)/(2b_0)$$ (4)

$$b_2 = 1 - (S_c)/b_0$$

where S_u, S_d, and S_c are the NRCS sampled in 20° degrees wide sectors in the upwind, downwind, and crosswind directions, respectively. The ECMWF wind speed and direction are taken as references for the binning process. The same computations have been done by using as a reference the scatterometer wind speed and direction in order to avoid as much as possible the effects of the reference wind errors. Computing the estimates in this manner makes no significant changes in the results (the two different estimates remain within their error bars).

The b_0 term (Figure 6a) is indicative of the NRCS wind speed dependency and shows a slower growth than is predicted by CMOD_IFR2. It confirms thus the tendency of the CMOD_IFR2 to underestimate the winds above 10 m/s. This effect is partly compensated by adding the bias term described in appendix. There is no indication on how it evolves above 20 m/s.

The b_1 and b_2 terms (Figures 6b and 6c) are indicative of the azimuthal modulation of the backscattering signal,

with b_1 related to the upwind/downwind asymmetry and b_2 related to the upwind/crosswind anisotropy. Like the b_0 term, the b_1 term reproduces the observations for moderate winds well and strongly overestimates the upwind/downwind asymmetry for high winds. As depicted by the theoretical models, upwind/downwind asymmetries arise mainly by the modulation of the short resonant Bragg waves by the long waves [Plant, 1986; Elfouhaily, 1997]. The degree of sea state development and long-wave-induced wind stress modulations are thus likely to influence the b_1 term. These effects are not well known and the observations do not provide any indication above 20 m/s.

The behavior of the b_2 term is well reproduced by CMOD_IFR2 for a broad range of wind speeds, but it is overestimated for the lowest incidence angles. Its decrease at high winds is reproduced, but there is still no indication of how it behaves above 20 m/s. There were not enough observations to calibrate CMOD_IFR2 in this wind speed range, and the b_2 term is thus constrained by the normalization of the wind speed applied in CMOD_IFR2 (see appendix). The upwind/cross-wind anisotropy is associated with the directionnality of the Bragg waves. We thus do not know if there are sufficient azimuthal NRCS modulations for wind speeds higher than 20 m/s to retrieve the wind direction with good accuracy.

At this point the question remains, whether there is sufficient modulation of the mean backscattering signal as a function of the wind speed and azimuth angle to estimate
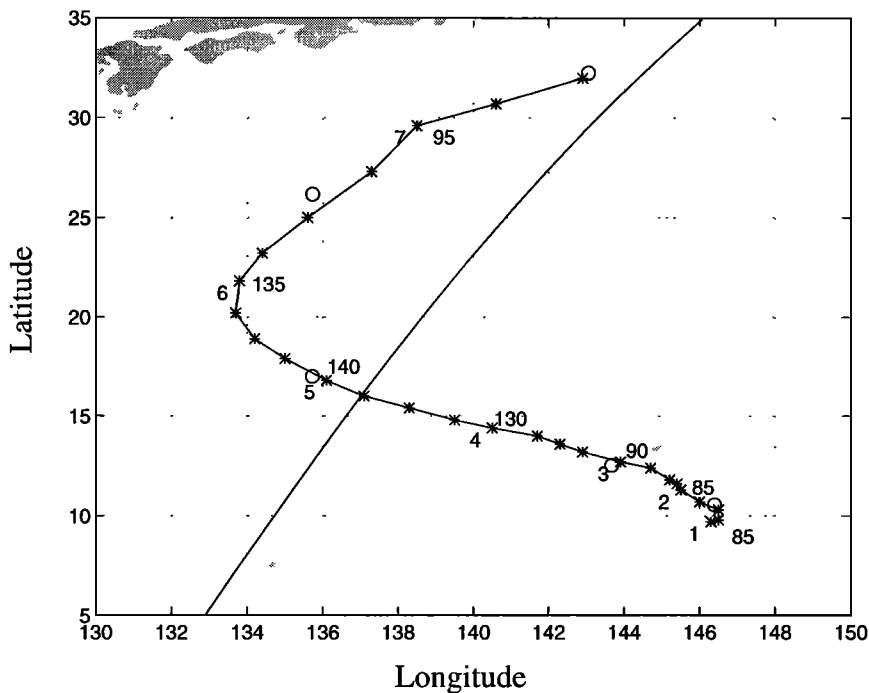
Figure 7. TC Elsie track as provided by the Joint Typhoon Warning Center (JTWC) every 6 hours (stars) from November 1 to November 7, 1992. The day numbers are indicated on the left, and the peak intensities in knots (1 knot = 0.5 m/s) are indicated on the right. The open circles indicate location of the TC center as derived from the ERS-1 scatterometer. The TOPEX-POSEIDON altimeter track intersects the TC track on November 4 at 1730 UTC.

the wind characteristics above 20 m/s. To investigate this topic, we propose in the following section to analyze qualitatively the surface microwave signature provided by different satellite sensors for the case of a tropical cyclone.

4.2. The Microwave Signature in Tropical Cyclone Elsie

4.2.1. Microwave signature of the ERS-1 scatterometer.
The case of TC Elsie (November 1992) was chosen because it was an average-sized, intense typhoon that was well sampled by ERS-1 and for which there was one track of the T/P altimeter near the center of the storm. There were also several SSM/I passes available from the F11 satellite. Figure 7 displays the location of TC Elsie every 6 hours, as determined by the Joint Typhoon Warning Center (JTWC) on Guams, together with the estimated maximum 1 min average sustained winds derived from the Dvorak [1976] satellite estimation method. The T/P altimeter swath and the positions of the TC center as determined from the ERS-1 scatterometer data are also shown. The TC locations from ERS-1 are found by locating the minimum high resolution wind speed in the TC center.

Elsie's track was directed west-northwest while the storm was intensifying until November 5 with a peak intensity of 150 knots (75 m/s). The recurvature occurred on November 6, after which Elsie accelerated toward the northeast and became an extra tropical storm on November 7. Between November 1 and 7, five ERS-1 scatterometer swaths sampled the cyclone.

As anticipated, ERS-1 computed wind speeds are much lower than the JTWC estimates (see Table 1). The following reasons can be given:

1. The scatterometer measurements are spatial averages over a footprint of about 25 km where strong gradients occur, while the maximum wind occurs a few tens of kms from the TC center, according to the Holland or Rankine profiles [Franklin et al., 1993]. The two estimates of the wind speed maximum are not strictly comparable because JTWC provides 1 mn local averages and due to their space/time separation. Nevertheless, they depict the same evolution of the TC intensity with a peak on November 5.

2. As outlined in section 4.1, the C band model overestimates the NRCS corresponding to high winds. The wind speed is therefore underestimated, and the sensitivity to increasing wind speed is too low for the very high wind speeds. This is illustrated in Table 1 where the maximum wind speed only increases by 2 m/s between November 3 and 5 when the 1 min average estimated by JTWC increases by 25 m/s.

3. Even though C band signals are not too strongly affected by atmospheric conditions, heavy precipitation and ice particles in the clouds may attenuate the NRCS signals and the rain droplets may also affect the sea surface roughness (wave damping). Such effects are hardly detectable without coincident measurements of the atmospheric parameters and because rainbands in TCs are generally also related to modification of the surface wind patterns [Anthes, 1982].

Table 1. Estimated Maximum Wind Speed According to ERS-1 Scatterometer HR Measurements for Five ERS-1 Passes and the Concurrent JTWC Wind Estimates

Date	Time, UTC	Peak Wind Speed, m/s	
		ERS	JTWC
Jan. 11, 1992	12 40	20.8	42.5
March 11, 1992	00 40	26.4	45.0
May 11, 1992	01 20	28 8	70.0
June 11, 1992	13 30	28.5	67.5
July 11, 1992	13 05	27.1	47.5

JTWC, Joint Typhoon Warning Center (Guam).

We will show that the dual-frequency altimeter T/P can be used to qualitatively estimate the influence of rain on the NRCS signal at C band.

The microwave signature of the sea surface in TCs is illustrated by Figures 8 and 9 with along-swath sections of the NRCS and wind speed at constant incidence angles as a function of the latitude, through the wind maximum and through the TC center. Two ERS-1 passes are shown occurring on November 3 (Figure 8) and on November 5 (Figure 9). These two passes correspond respectively to the intensifying and to the mature phases of Elsie, stages where the wind gradients and intensities are the highest. On November 3, the incidence angles of the NRCS sections are 36.4° and 38.5°, respectively, through the TC maximum and through the TC center. On November 5, there is only one NRCS section at 35.7° incidence angle crossing the TC center as well as the TC maximum (see Plate 2 to locate the sections). To meaningfully describe the microwave signatures, the following quantities S_1 and S_2 have been used rather than the individual NRCS for each antenna:

$$S_1 = (\sigma_1 + \sigma_3)/2 \approx b_0 \qquad (5)$$
$$S_2 = (\sigma_1 - \sigma_3)/(\sigma_1 + \sigma_3) \approx b_2 \times \cos 2\phi$$

where σ_1 and σ_3 are the NRCS for the lateral antennae, ϕ is the wind direction relatively to the central antenna and b_0 and b_2 are the model parameters as already described in section 2.

These quantities are first-order approximations, assuming a negligible upwind/downwind difference, i.e., that $b_1 \ll 1$. S_1 does not depend on the wind direction, the two lateral antennae being separated by 90°, and is thus indicative of the behavior of the NRCS as a function of the wind speed. S_2, designed as the anisotropy coefficient, characterizes the NRCS azimuthal anisotropy. It depends mainly on the wind direction and depends slightly on the wind speed only through b_2 as shown in Figure 6c. A maximum in S_2 corresponds to an upwind or downwind (crosswind) case for the forebeam (aft beam), and a minimum corresponds to a crosswind (upwind or downwind) case for the forebeam (aft beam).

Computations are carried out for the HR as well as for the LR scatterometer measurements. One can make the following observations:
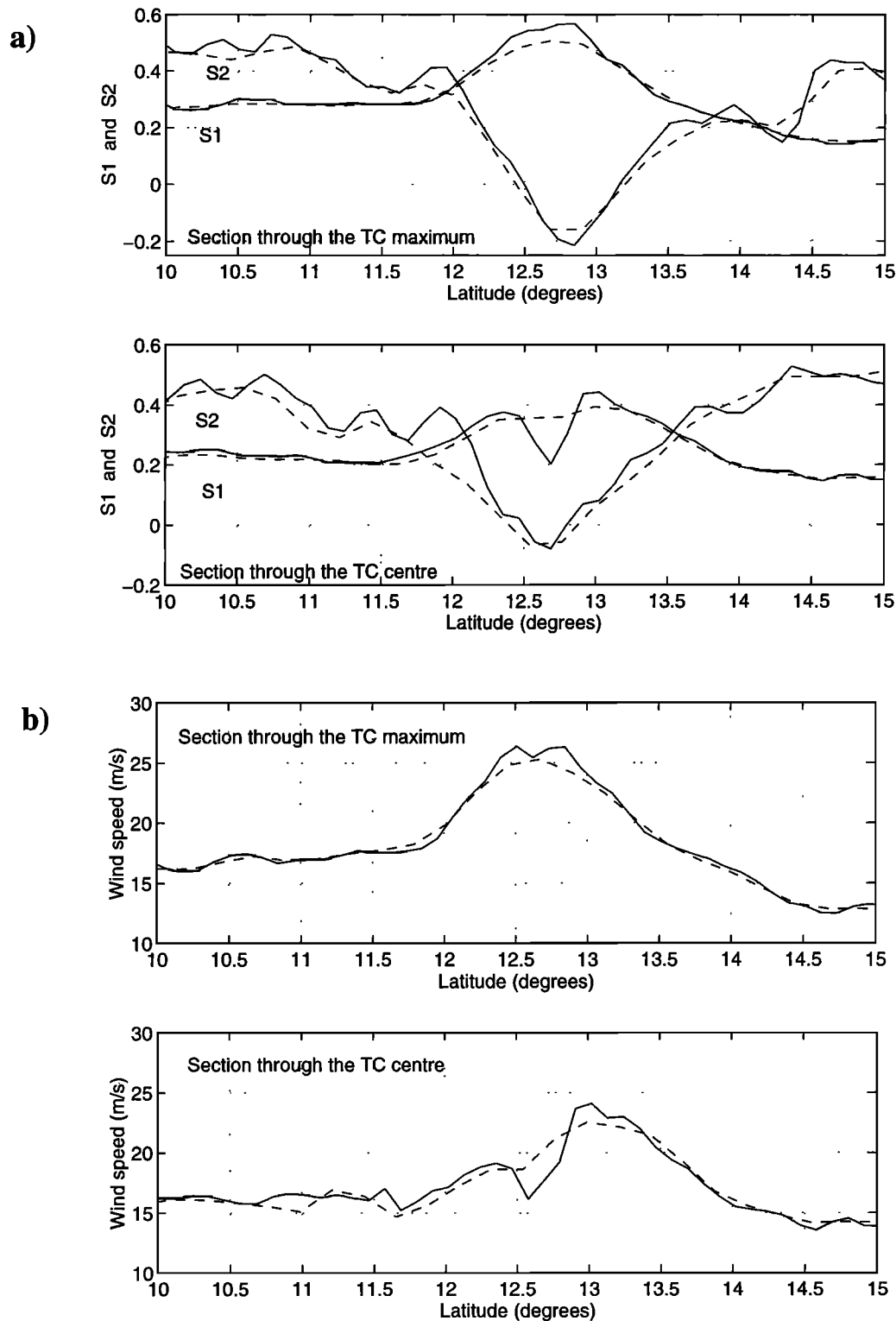
Figure 8. Sections of (a) S_1 and S_2, (b) wind speed, (top) through the region of maximum winds (incidence 36.4°) and (bottom) through the TC center (incidence 38.5°) on November 3, 1992. Solid and dashed lines are for the high- and low-resolution modes, respectively.

1. In the sections crossing the TC wind maxima (top panel of Figure 8a, and Figure 9a), S_1 changes smoothly on both sides of the TC and does not exhibit a saturation at the maximum level. The NRCS are significantly greater for the HR, meaning that taking a spatial average is of concern at such high wind speeds. The HR allows better representation of the sea surface roughness variability, but it is not accompanied by a great difference in the maximum wind speed between the HR and LR measurements owing to the lack of sensitivity of the C band model (Figure 8b and 9b).
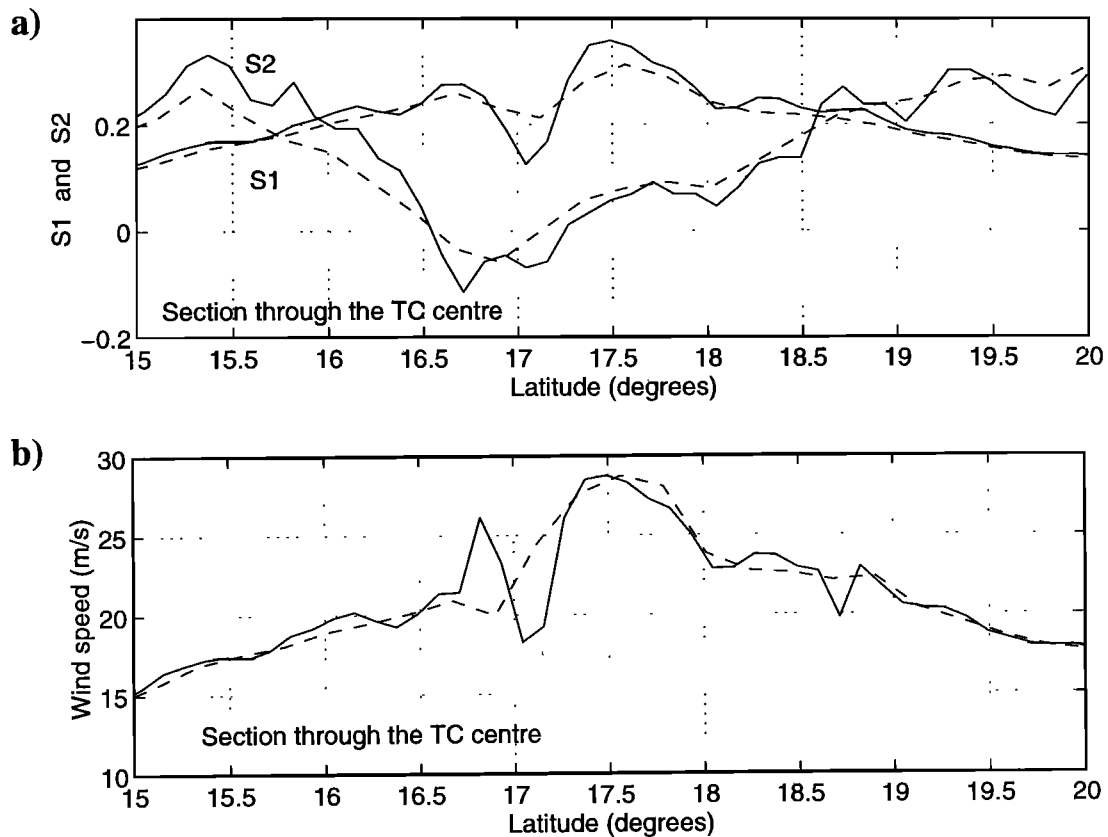
Figure 9. Sections of (a) S_1 and S_2, (b) wind speed as a function of the latitude, through the TC center (also the region of maximum winds, incidence 35.7°) on November 5, 1992. Solid and dashed lines are for the high- and low-resolution modes, respectively.

The coefficient of anisotropy, S_2, exhibits a variability mainly linked to the wind direction variability. On November 3, in the area of maximum winds (above 20 m/s between 12°N and 13.5°N), S_2 varies from a value of 0.4 (wind direction upwind for the forebeam or cross-swind for the aft beam) at 12°N to a value of -0.2 (wind direction upwind for the aft beam or cross-wind for the forebeam) at 12.8 N. It means that the upwind forebeam NRCS is roughly 7% or 2.4 dB higher than the cross-wind aft beam value at 12°N (wind speed about 20 m/s) and the upwind aft beam NRCS is 50% or 1.8 dB higher than the cross-wind forebeam value at 12.8°N (wind speed > 25 m/s). These values for a wind speed of 20 m/s are of the same order as those provided by CMOD_IFR2 for medium wind speeds, showing therefore still a sufficient azimuthal modulation. If the physical basis of the azimutal anisotropy is relatively well understood for moderate winds, it is not obvious what scattering mechanism dominates at the sea surface under the extreme conditions that occur in TCs. The well-defined behavior of the NRCS measurements in TCs is very encouraging and can explain why patterns of retrieved wind fields fit to known wind patterns of TCs (Plate 2).

2. In the sections crossing the TC centers (bottom panel of Figure 8a, and Figure 9a), the previous remarks also hold. Moreover, a striking feature is the notable difference between the HR and LR measurements. Indeed if the TC cen-

ter is well delineated by a drop in the HR values of S_1 on November 3 (bottom panel of Figure 8a near 12.7°N) and on November 5 (Figure 9a near 17.1°N), it is drastically smoothed in the LR measurements. It is also shown in the wind speed patterns (Figures 8b and 9b) for which significant differences appear between the HR and LR patterns. It appears that the 25 km resolution is critical to retrieve the main TC wind pattern characteristics.

In summary, the scatterometer NRCS signal still exhibits a very well defined modulation in the regions of maximum winds and in the center of an intense typhoon, allowing retrievial of the wind vector patterns. Additionally, it is shown that the HR measurements allow a smaller scale microwave signature in TCs and thus improvement of the description of the TC structure. Nevertheless, the scatterometer transfer function is not really calibrated for such extreme conditions. Moreover, the influence of heavy rain or ice particles on the ERS-1 C band scatterometer signal is not known and may be responsible in part for the underestimation of the maximum winds.

In the following section we analyze the microwave signature of the T/P altimeter in order to provide another perspective on the problems mentioned above.

4.2.2. Microwave signature of the TOPEX-POSEIDON altimeter. The dual-frequency T/P altimeter obtains C band and Ku band NRCS measurements at nadir (No-
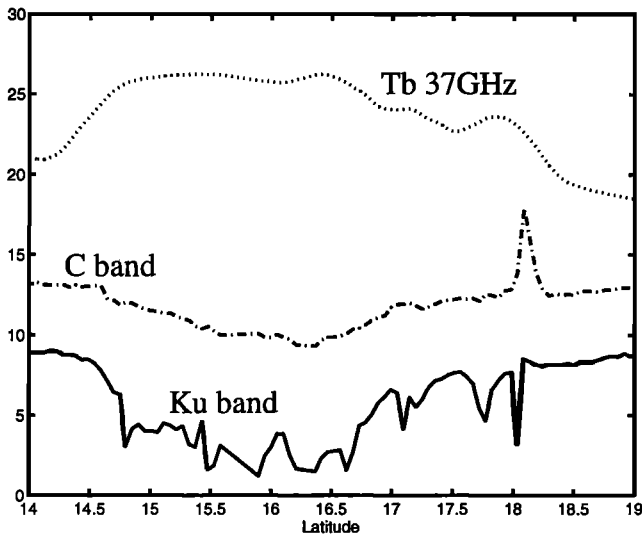
Figure 10. TOPEX-POSEIDON altimeter data near Tropical Cyclone Elsie: NRCS in Ku band (solid) and in C band (dashed-dotted), in decibels; TMR brightness temperature at 37 GHz (dotted), in units of 0.1x °K. High modulation is observed in Ku band while C band is still smoother. The TMR brightness temperature increases near the cyclone for the latitudes 14° to 19°N.

vember 4, 1992, 1730 UTC), just a few kms ahead of Elsie's center (see Figure 7 and Plate 1).

4.2.2.1. Atmospheric effects: Figure 10 displays the NRCS values, together with the T/P Microwave Radiometer (TMR) brightness temperatures at 37 GHz, near the TC center (around 16°N). Altimeter NRCS values at C band and Ku band decrease towards the TC center and are related mainly to increasing wind speed. The Ku band σ_0 decreases more and faster than the σ_0 at C band, but it is not clear if this is due to a greater sensibility to the sea surface roughness or to greater interactions with the atmospheric precipitation and cloud particles. There is much more small-scale variability, of the order of a few tens of kms, in the Ku band signal. It can be hypothesized that this variability is due to large attenuation of the signal at Ku band by rain cells or ice particles. The altimeter has lost the signal near the outer convective band (Plate 1) at 18°N, and the σ_0 measurements are thus erroneous at this location. At this location both NRCS signals and also the significant wave height (not shown) have large deviation from the mean behavior, but they deviate in opposite directions. This behavior was observed earlier in T/P altimeter measurements by *Tournadre and Morland* [1997].

If the C band signal is also likely to be affected by atmospheric particles or by the effect of rain droplets on the sea surface roughness, a strong or systematic influence is not discernible as it is in the Ku band signal. With the exception of the anomaly described above, we observe that the TMR brightness temperatures increase with decreasing NRCS, but the TMR resolution of 35 km does not allow examination of the small scale variability in the atmospheric param-

eters. In order to better analyze the relationship between the NRCS and the rain events, we have collocated the T/P data in space and time with the 85 Ghz brightness temperatures of the SSM/I for November 4, 1992, 2010 UTC (Plate 1). Estimation of the rain rate is not available because it requires an estimation of the wind speed and the SSM/I wind algorithms are no longer valid for high levels of liquid water content. Nevertheless effects of hydrometeors on the brightness temperatures at these frequencies result in a depolarization of the signal [*Petty*, 1994], and thus the vertically and horizontally polarized signals are used to compute an index of depolarization. After it has been normalized by the effects of the water vapor content and surface wind speed in the environment, it is defined as the normalized difference of the two channels. It can be used as an indicator of rain/no rain occurrence in the cells. These variables are displayed in Figure 11. The brightness temperatures decrease from a latitude of 14°N toward a minimum corresponding to the temperature at the top of the clouds in the eyewall region where the surface convergence and atmospheric water content are maximum. Then they increase in the vicinity of the TC center near 16°N and decrease again on the north side of the TC. Farther north (18°N) there is another minimum of temperature corresponding to an outer rainband and where the altimeter NRCS signal at Ku and C bands are obviously contaminated. The SSM/I index of depolarization is also displayed in Figure 11. It has two major maxima (signal totally depolarized) on both sides of the TC center, indicating the possible occurrence of heavy rains surrounded by large ice particles, and a third one in the rainband area. The index exhibits small scale variations elsewhere. To give more consistency to this analysis, we now relate this index to another rain index derived from the
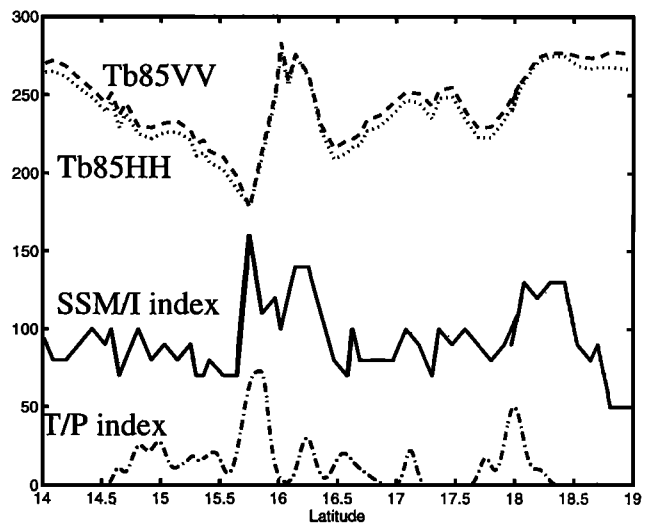
Figure 11. Collocated TOPEX-POSEIDON and SSM/I measurements. Brightness temperature at 85 GHz VV-pol (dashed) and HH-pol (dotted) in degrees Kelvin, SSM/I scaled polarization difference (solid), and TOPEX-POSEIDON rainfall index (dashed-dotted).
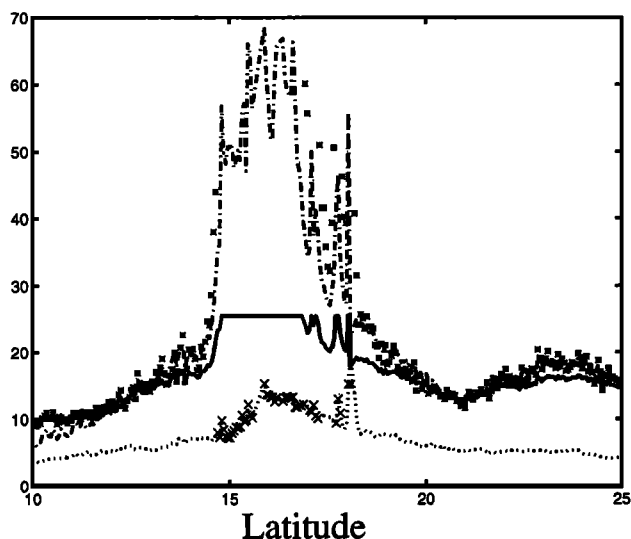
Figure 12. Wind speed (m/s) estimation from the single-frequency algorithms of *Witter and Chelton* [1991] (solid) and of *Young* [1993] (dashed-dotted) and the dual-frequency algorithm of *Elfouhaily* [1996] (asterisks). The Ku band significant wave height (SWH in meters) is also given for reference (dotted). The cross characters are data points for which Elfouhaily's algorithm did not converge. Between the latitudes of 15° and 18°N, convergent and divergent points are interlaced, which seems to indicate that rain cells induce differences from the Ku/C band relationship for no-rain conditions and therefore these situations result in numerically non converging calculations for the dual-frequency wind algorithm.

analysis of T/P echo waveforms and also displayed in Figure 11. This latter index is based on the Ku band NRCS departures from the mean Ku band/C band relationship [*Chapron et al.*, 1995]. *Tournadre and Morland* [1997] have thoroughly examined many cases of T/P altimeter measurements in the presence of rain and have concluded that the Ku band NRCS are lowered in nearly all cases when the C band signal exhibits a lowering or an increase only in a few cases. Thus they have defined a rain index, to be used as a rain flag, that is related to the departure of the Ku band signal from the mean Ku band/C band relationship, the later having been defined for no rain cases. As displayed in Figure 11, this index indicates a variability that is qualitatively well related to the SSMI index, even if errors in the collocation, the sensor resolutions and sampling, and if geophysical effects induce differences in the exact location of the maxima that are seen by the two indices. It appears that there is a close relationship between the small scale drops in the NRCS signal at Ku band and the peaks of the SSM/I depolarization index, showing that the Ku band NRCS are strongly contaminated by the atmospheric particles.

We then note that the C band signal is not so much contaminated by atmospheric particles, unlike the Ku band sig-

nal, and that it is possible to retrieve the wind structures with a relatively good accuracy even in these extreme events. This is also illustrated by the examples of the retrieved wind fields shown in Plate 2. They are quite consistent, and no obvious sign of contamination is visible.

4.2.2.2. A high-wind branch for the C band model: As outlined in the previous sections, the C band model sensitivity is too low to display the high wind variability. This behavior was also observed on the altimeter winds. In most of the cyclone cases, the wind exceeds the upper limit of wind speed (20 m/s) imposed by altimeter inversion algorithms whose calibration is based upon buoy measurements. On the basis of parametric model predictions [*Holland*, 1980] of the surface winds in TCs, *Young* [1993] developed a hurricane algorithm for the Geosat altimeter (Ku band) whose validity ranges from 20 to 40 m/s. This algorithm is only applicable to altimeter measurements that are not highly attenuated by the presence of hydrometeors in the atmosphere. Unfortunately, hurricane winds are highly correlated with precipitation in tropical cyclones. Therefore use of Young's algorithm to estimate high winds must be restricted to cases where precipitation does not significantly affect the altimeter measurements. As was already shown by *Tournadre and Morland* [1997] the Ku/C band relationship for T/P is a good indicator of rain in tropical cyclones. In addition, a recent study conducted by *Elfouhaily* [1996] demonstrated the ability to estimate a sea state dependent local wind speed using the same Ku/C band relationship. The later was called local wind speed because of its dependence on the local sea state. Figure 12 shows that the local wind speed is comparable to the one from *Witter and Chelton* [1991] for winds lower than 15 m/s and with winds from *Young* [1993] otherwise. For latitudes between 15°N and 18°N the dual frequency based algorithm features the ability to discriminate between measures without significant atmospheric contamination and measures affected by a strong attenuation of the Ku band NRCS. As hypothesized, this attenuation is always attributed to rain cells present during the altimeter pass.

The inclusion of C band estimation in the dual-frequency algorithm thus helped both the estimation of the wind and the detection of an excessive attenuation of the Ku band in the presence of rain.

Direct application of altimeter findings to scatterometers for high-wind estimations is not a straightforward manipulation mainly because of the differences in range of incidence angles at which these instruments operate. However, when one looks more closely to the scattering mechanism involved in both configurations, possible transition may be envisaged. Indeed, differences between C and Ku band altimeter measurements may be associated with different cut-off wavelengths that separate long and short scales on the surface: the real surface appears smoother to larger microwave wavelength [*Chapron et al.*, 1995]. For C and Ku band radars, well-accepted cut off values are about 3 times the incident electromagnetic wavelength [*Brown*, 1990], 16 cm and 6 cm, respectively. Therefore differences between C and Ku band measurements are then mainly dominated by small scale slope and height variances covering the

85 GHz SSMI Brightness Temperatures (°K, VV–pol) 4–NOV–1992 20:02 UTC
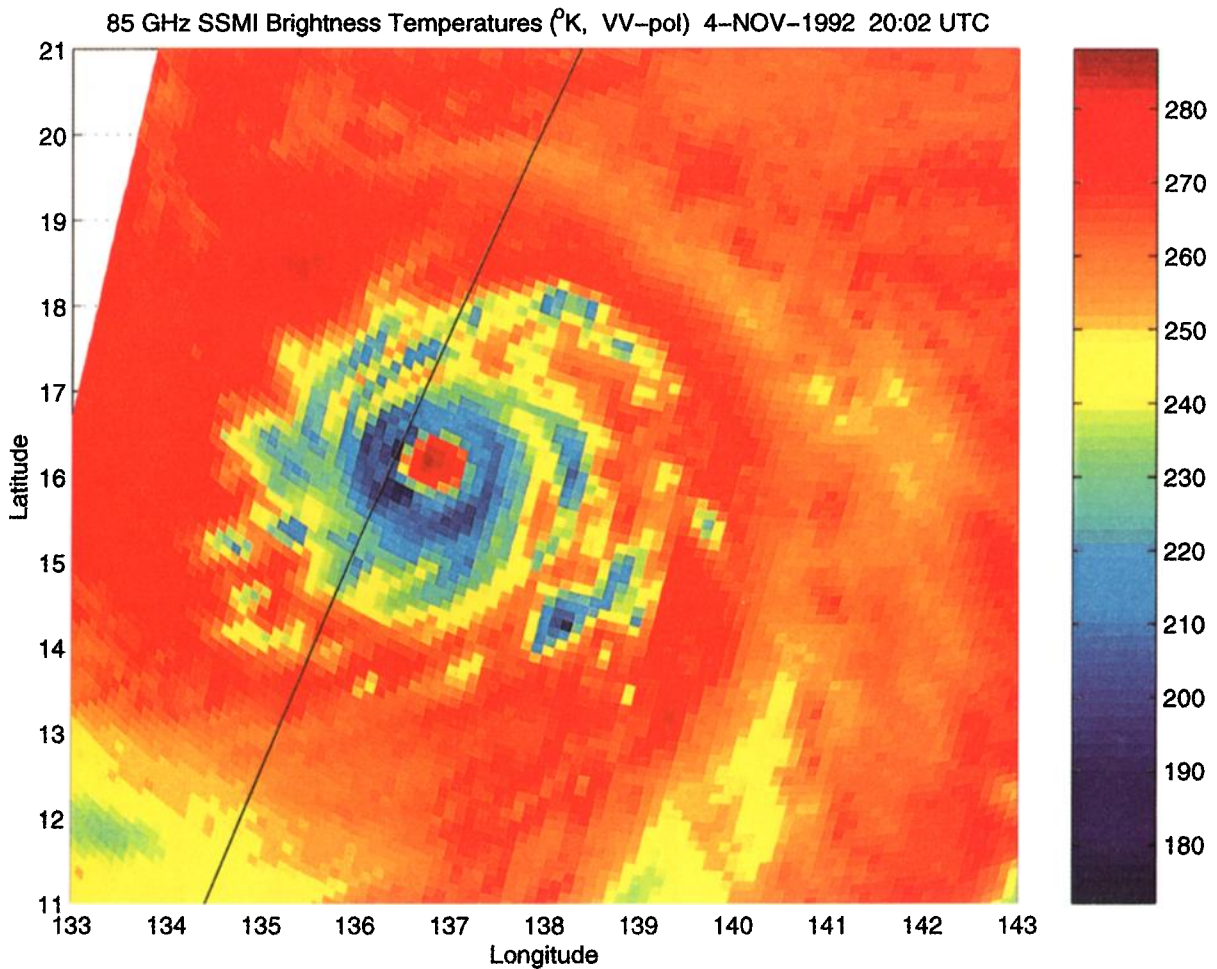
Plate 1. SSM/I 85 GHz brightness temperatures in degrees Kelvin (November 4, 1992, 2002 UTC), and the TOPEX-POSEIDON altimeter ground track (November 4, 1992, 1730 UTC). The altimeter positions have been shifted in order to take the time differences into account.

range of centimetric waves (from 6 to about 16 cm). Such a range is also preponderant for C band off nadir scatterometer measurements. We can then envisage to construct a high-wind branch for the C band scatterometers based on the high-wind branch of the altimeter algorithm. The possible methodology would be to collocate ERS scatterometer measurements with dual-frequency altimeter ones close to hurricane winds (after elimination of anomalous Ku band measurements).

5. Examples of Surface Wind Patterns in Tropical Cyclones

The knowledge of surface wind patterns in TCs is of great importance to understanding and forecasting the formation and the evolution of cyclones. If the physics of mature cyclones are rather well known, there remain many uncertainties regarding how TCs develop and what the atmospheric conditions are that enable or inhibit intensification of a tropical disturbance. Currently, there is a dramatic lack of three-dimensional measurements of most of the parameters of interest. Observations by scatterometers pro-

vide a unique view of the surface wind patterns in the outer core of TCs with a good resolution and of the surface wind of the environmental flow embedding the TC. We intend in this section to discuss the features delineated by the scatterometer in a few cases, in order to assess this new data source and its usefulness.

Plate 2 displays the HR surface winds in TC Elsie for four ERS-1 passes where the TC core was identified. Elsie's track determined by JTWC and location of its center determined with ERS-1 scatterometer are shown in Figure 7. Elsie was moving west-northwest away from Guam on November 3, 1992, while intensifying until November 5, when it reached its peak intensity of 150 knots (75 m/s). It turned north-northeast later that day and accelerated on November 6 while weakening. Then it turned east-northeast and became a typhoon-force extratropical low on November 7. During this period the region of maximum winds in the outer radius grew from about 100 km to several hundred of kilometers. One striking feature is strong asymmetries in the surface winds as displayed in Plate 2. Asymmetries in TCs have been previously documented [*Holland*, 1980; *Anthes*, 1982; *Quilfen et al.*, 1994; *Franklin et al*, 1993]. They

3 Nov.

5 Nov.

6 Nov.

7 Nov.

2 6 10 14 18 22 26 30
Wind speed m/s
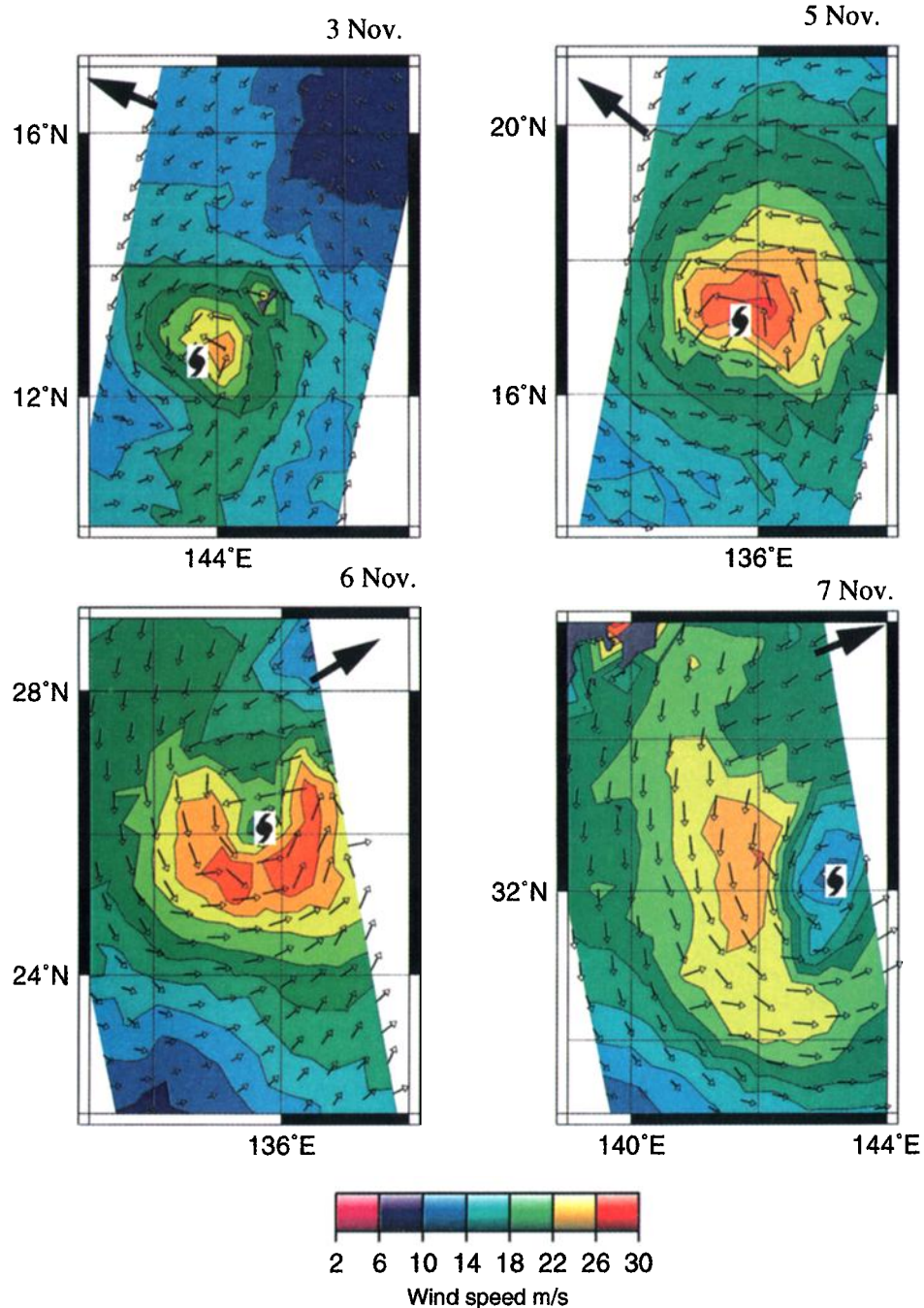
Plate 2. Surface wind field from the ERS-1 scatterometer at a resolution of 25 km in tropical cyclone Elsie: (a) November 3, (b) November 5, (c) November 6, and (d) November 7, 1992. Location of the TC center determined from the scatterometer measurements and the TC direction are indicated.

are related to the movement of the axisymmetric vortex in the environmental flow but also to many other mechanisms. They partly organize the distribution of convection and are a characteristic feature of the tropical cyclone evolution. The maximum winds are on the right side of the typhoon moving northwestward on November 3 and 5 and also on the right side of Elsie as it moved northeastward on November 6. The position of the maximum winds reversed after Elsie's recurvature. This distribution could be due to more prevailing easterlies in the south part and more prevailing

westerlies in the north part. This characteristic has been observed in many of the TCs sampled by the ERS-1 scatterometer, and is in agreement with previous studies. *Franklin et al.* [1993] outlined a similar distribution of surface winds by using nested analyses of Hurricane Gloria in the Atlantic Ocean.

Figure 13 displays the surface wind divergence fields for a few cases of mature or intensifying TCs. It features characteristic patterns of the wind divergence that are nearly the same in all cases. Strong convergence occurs in the south
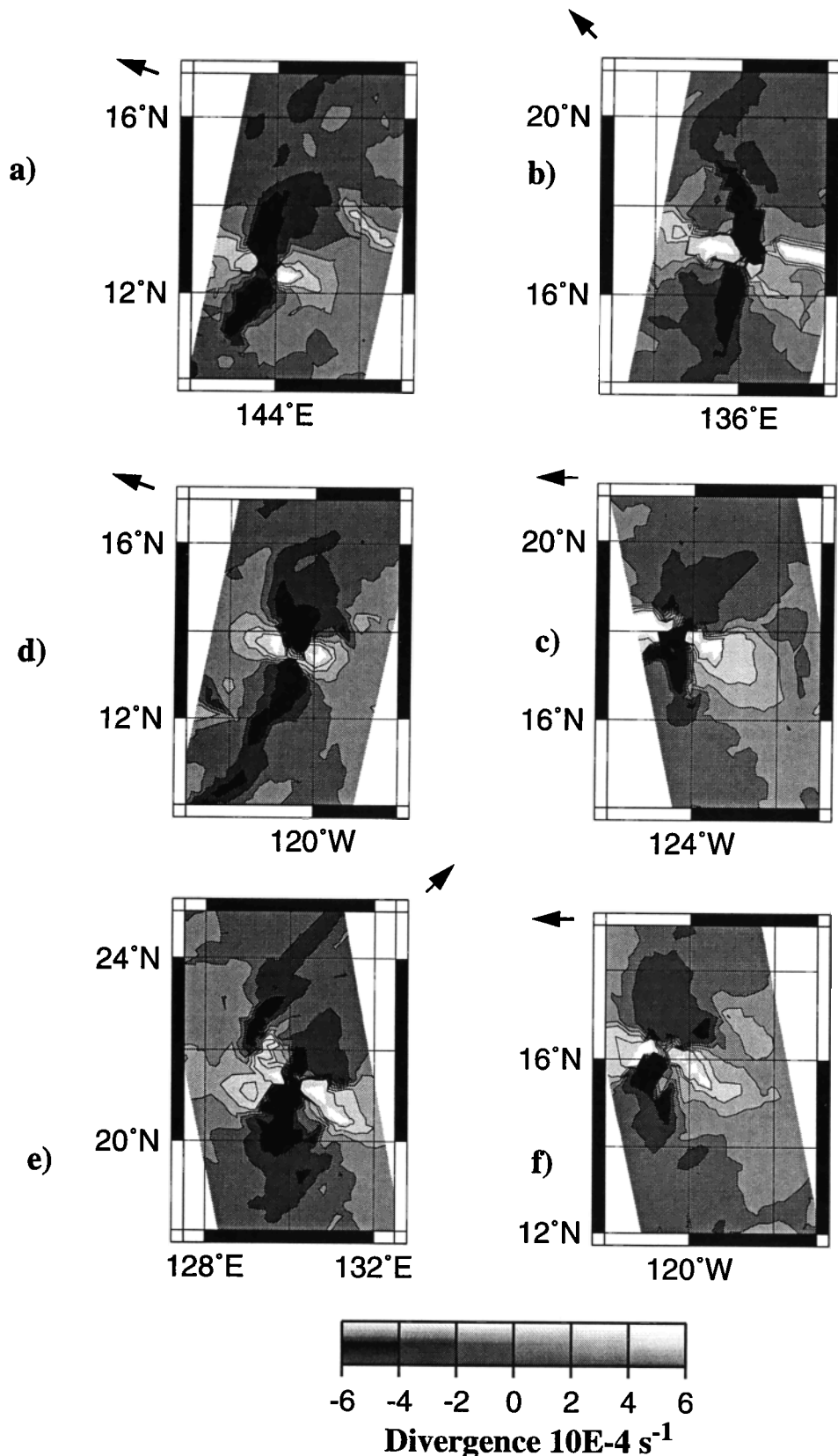
Figure 13. Surface wind divergence in (a) TC Elsie, November 3, 1992; (b) TC Elsie, November 5, 1992; (c) TC Tina, October 2, 1992; (d) TC Orlene, September 5, 1992; (e) TC Yvette, October 14, 1992; and (f) TC Frank, July 18, 1992. The arrows indicate the direction of the TC track.

and north parts of the TCs and the flow is divergent in the other quadrants. *Anthes* [1982] noted that surface wind convergence occurs in the vicinity of rainbands with values exceeding 4×10^{-4} s^{-1}. It is also the order of magnitude of the ERS-1 wind divergence. Nevertheless, it was shown by *Ebuchi* [1994] that the scatterometer antenna geometry, imperfections in the backscattering models, and processing algorithms could produce wind direction trapping in favored directions aligned with the antennae. To verify whether or not these divergence structures are artifacts, we have simulated the NRCS as observed by the ERS scatterometer in a perfectly symmetric vortex. We have then retrieved the wind field and computed its divergence. Patterns similar to those shown in Figure 13 also occur, showing that the retrieved features are partly artifacts related to the antenna geometry. It is thus hardly possible to delineate the true geophysical divergence field from these artifacts.

6. Conclusion

The wind fields derived from 29 orbits of ERS-1 scatterometer measurements at high (25 km) and low (50 km) resolutions have been analyzed for a few tropical cyclone events. Increasing the resolution enables to greatly reduce the geophysical noise in the measurement cells, and thus to improve the NRCS estimates. Such an enhancement for the measurement definition is due to the high instrument signal to noise ratio: the radiometric resolution does not dominate the noise budget.

Examining the surface wind structures in tropical cyclones, we show that usable ERS scatterometer data are obtained, even through deep convective clouds. Three main shortcomings of scatterometry for remote sensing of such events were identified as follows:

1. The measurement resolution as discussed above is only 50 km for the operational ERS scatterometer activities. It is too coarse to measure the wind structures that vary typically over a few kms; NRCS measurements are dramatically smoothed in the vicinity of the TC centers. The knowledge of these small scale structures is of great interest for TC forecasting and physical modeling. It is shown that the higher resolution of 25 km providing measurements every 12.5 km retains some of the main characteristics of the surface wind patterns such as the location of the TC center with its area of low winds, the location of the outer core maximum winds and its radius to be featured. A 25 km (or even better) resolution is critical for measuring the surface wind structures with sufficient accuracy to help to understand the TC mechanisms and to improve the estimates of wind radii and storm surge forecasting.

2. Heavy rain is likely to interact with a microwave signal. The C band signal is theoretically only weakly affected by rain through its path in the atmosphere, but little is known about effects of heavy rains (both on the sea surface roughness and on the C band signal itself) that are permanent features of TCs. To provide a qualitative insight on this topic, we have analyzed the backscattered signals of the T/P dual-frequency altimeter for one track crossing Elsie's core. The NRCS at Ku band exhibits drops that are strongly linked to the variability of a rain index derived from the SSM/I high-frequency brightness temperatures. At the same time, the C band signal does not exhibit such a variability at this scale, and it is thus confirmed that the C band NRCS are not too seriously contaminated by rain. Moreover, this result supports the usefulness of a rain index, derived from the T/P altimeter, based upon the deviation of the Ku signal from a mean C band/Ku band relationship.

3. Very little is known about the behavior of the scatterometer signal for very high winds, and the C band backscattering model is less valid for winds above 20m/s. Estimation of these winds by using the operational backscattering models gives very crude estimates of the mean wind level even if such estimates provide some information on the wind variability. It is clear that NRCS for high winds are overestimated by the existing models, leading to an underestimation of the wind speeds. An examination of the NRCS signals in TCs shows that the mean backscattered signal does not appear to saturate and exhibit sufficient azimuthal modulation in the most intense tropical cyclones, with a superior sensitivity for the highest resolution. Previous work developing altimeter wind algorithm for higher winds are illustrated for a T/P track analyzed in this paper. We propose that an analogous approach may be used to define a high-wind branch for the scatterometer C band model.

With these limitations in mind, the surface winds are analyzed in TC Elsie. The most prominent features are the asymmetries existing in the wind speed field and the well-defined patterns in the divergence field. The location of the wind maximum appears to occur mainly on the right side of the moving storm, a feature that was previously identified by different authors on the basis of observational and theoretical work. This is hypothesized to be mainly due, among other mechanisms, to the displacement of the storm in an environmental flow with a prevailing surface wind direction. Another characteristic feature is the distribution of the wind divergence, strong convergence patterns being identified on the south and north sides of most of the studied TC cases. However, a simulated test shows that the convergence patterns delineated by the scatterometer are partly artifacts of the antenna geometry, thus limiting their interpretation.

To conclude, the scatterometer data source of surface winds is very promising but much work is still to be done in order to interpret scatterometer signals at C band and Ku band. Such studies will help to better understand the characteristic wind patterns of tropical cyclones as measured by scatterometry. The forthcoming operational scatterometers on-board the ADEOS (Ku band) and METOP (C band) satellites will provide at least twice as many complementary measurements with a better resolution than the ERS operational one and should contribute strongly in the near future to better understanding and forecasting of tropical cyclones. Continued improvment of the interpretation of the scatterometer signals in tropical cyclones is therefore of great importance, especially because these data are already used by forecasters.

Appendix

A1. The Backscattering Model CMOD_IFR2

The backscattering model CMOD_IFR2 is formulated as follows:

$$\sigma_0 = 10^{\alpha + \beta\sqrt{V}} \times (1 + b_1 \times \cos\Phi + \tanh b_2 \times \cos 2\Phi)$$

$$\text{(A1)}$$

where tanh is the hyperbolic tangent, with

$$\alpha = c_1 + c_2 P_1 + c_3 P_2 + c_4 P_3$$
$$\beta = c_5 + c_6 P_1 + c_7 P_2$$

where

$$P_1 = x \qquad P_2 = (3x^2 - 1)/2 \qquad P_3 = x(5x^2 - 3)/2$$

$$x = (\theta - 36)/19$$

and

$$b_1 = c_8 + c_9 V_1 + c_{10} P_1 + c_{11} P_1 V_1 + c_{12} P_2 + c_{13} P_2 V_1$$

$$b_2 = c_{14} + c_{15} P_1 + c_{16} P_2 + (c_{17} + c_{18} P_1 + c_{19} P_2) V_1$$
$$+ (c_{20} + c_{21} P_1 + c_{22} P_2) V_2 + (c_{23} + c_{24} P_1 + c_{25} P_2) V_3$$

where

$$P_1 = x \qquad P_2 = 2x^2 - 1 \qquad x = (2\theta - 76)/40$$

$$V_1 = (2V - 28)/22 \qquad V_2 = 2V_1^2 - 1 \qquad V_3 = (2V_2 - 1)V_1$$

σ_0 is the normalized radar cross section, V is the wind speed in meters per second, ϕ the wind direction in degrees relative to the antenna, and θ the incidence angle in degrees. Parameters values and test values are given in Tables A1 and A2.

A2. High Wind Bias Correction

After the wind speed V_m has been computed from the C band model, the following bias correction is added:

Table A1. Parameter Values

Parameter	Value	Parameter	Value
c_1	-2.437597	c_{14}	0.412754
c_2	-1.567031	c_{15}	0.121785
c_3	0.370824	c_{16}	-0.024333
c_4	-0.040590	c_{17}	0.072163
c_5	0.404678	c_{18}	-0.062954
c_6	0.188397	c_{19}	0.015958
c_7	-0.027262	c_{20}	-0.069514
c_8	0.064650	c_{21}	-0.062945
c_9	0.054500	c_{22}	0.035538
c_{10}	0.086350	c_{23}	0.023049
c_{11}	0.055100	c_{24}	0.074654
c_{12}	-0.058450	c_{25}	-0.014713
c_{13}	-0.096100		

Table A2. Test Values

V, m/s	Φ, deg	θ, deg	σ_0, dB
1	0	60	-31.84
1	90	60	-32.81
8	0	40	-14.45
8	90	40	-19.02
15	0	25	-2.57
15	180	25	-2.71
22	0	18	4.38
22	180	18	5.32
28	0	18	4.74
28	180	18	6.19

$$V_{scat} = V_m + V_{bias} \qquad \text{(A2)}$$

with

$$V_{bias} = 0 \qquad \text{if } V \leq 10 \text{ m/s}$$

$$V_{bias} = 0.0831 \times V_m - 0.0173 \times V_m^2 + 0.0009 \times V_m^3$$
$$\text{if } 10 < V \leq 22 \text{ m/s}$$

$$V_{bias} = \arctan(V_m - 22) + 3.0382 \qquad \text{if } V > 22 \text{ m/s}$$

The function arctan designs the arctangent.

The bias was evaluated by comparison of the C band model winds with the NOAA buoys winds for the time period March 1992 to October 1993.

References

Anthes, R.A., *Tropical Cyclones, Their Evolution, Structure and Effects, Meteorol. Monogr. Ser.*, Vol. 19, No. 41, 208 pp, Am. Meteorol. Soc., Boston, Mass., 1982.

Archiving, Validation and Interpretation of Satelite data in Oceanography (AVISO), *AVISO User Handbook: Merged TOPEX/POSEIDON Products, Rep. AVI-NT-02-101-CN*, edition 2.1, 208 pp, Centre National d'Etudes Spatiales, Toulouse, France, 1992.

Bentamy, A., Y. Quilfen, P. Queuffeulou, and A. Cavanie, Calibration of the ERS-1 scatterometer C-band model, *Tech. Rep. IF-REMER DRO/OS-94-01*, 72 pp, Inst. Fr. de Rech. pour l'Exploit. de la Mer, Plouzané, France, 1994.

Brown, G.S., Quasi-specular scattering from the air-sea interface, in *Surface Waves and Fluxes*, vol. 2, edited by G.L. Geernaert and W.J. Plant, pp 1-39, Kluwer Acad., Norwell, Mass., 1990.

Chapron, B., K. Katsaros, T. Elfouhaily, and D. Vandemark, A note on relationships between sea surface roughness and altimeter backscatter, in *Air-Water Gas Transfer*, pp. 869-878, Heidelberg Univ., Heidelberg, Germany, 1995.

Dvorak, V.F., Tropical cyclone intensity analysis and forecasting from satellite imagery, *Mon. Weather Rev.,* 103, 420-430, 1976.

Ebuchi, N., Directional distribution of wind vectors observed by ERS-1 scatterometer, in *Proceedings 2nd ERS-1 work*shop, *Tech. Rep. IFREMER DRO/OS/94-06*, pp 89-92, Inst. Fr. de Rech. pour l'Exploit. de la Mer, Plouzané, France, 1994.

Elfouhaily, T., Modèle couplé vent/vagues et son application à la télédétection par micro-onde de la surface de la mer, 229 pp., Thèse de Doctorat , Univ. Pierre et Marie Curie, Paris, 1996.

Elfouhaily, T., B. Chapron, K. Katsaros, and D. Vandemark, A unified directional spectrum for long and short wind-driven waves, *J. Geophys. Res., 102*, 15781-15796, 1997.

Emanuel, K. A., The maximum intensity of hurricanes. *J. Atmos. Sci., 45*, 1143-1155, 1988.

Fischer, R. E., Standard deviation of scatterometer measurements from space, *Proc. IEEE, 10*, 106-113, 1972.

Franklin, J.L., S.J. Lord, S.E. Feuer, and F.D. Marks, The kinematic structure of Hurricane Gloria (1985) determined from nested analyses of dropwindsonde and Doppler radar data, *Mon. Weather. Rev., 121*, 2433-2451, 1993.

Freilich, M. H., and R. S. Dunbar, A preliminary C-band scatterometer model function for the ERS-1 AMI instrument, in *Proceedings of First ERS-1 Symposium: Space at the Service of Our Environment, Eur. Space Agency Spec. Publ., ESA SP-359*, pp. 79-83, March 1993.

Graber, H. C., N. Ebuchi, and R. Vakkayil, Evaluation of ERS-1 scatterometer winds with wind and wave ocean buoy observations, *Tech. Rep. RSMAS 96-003*, 69 pp, Rosentiel School of Mar. and Atmos. Sci., Univ. of Fla.. Miami, 1996.

Gray, W.M., Tropical cyclone formation and intensity change, paper presented at ICSU/WMO International Symposium on Tropical Cyclone Disasters, Int. Counc. of Sci. Unions, Beijing, 1993.

Holland, G.J., An analytical model of the wind and pressure profiles in hurricanes, *Mon. Weather Rev., 108*, 1212-1218, 1980.

Jones, W.L., L.C. Schroeder, D.H. Boggs, E.M. Bracalente, R.A. Brown, G.J. Dome, W.J. Pierson, and F.J. Wentz, The Seasat-A satellite scatterometer: The geophysical evaluation of remotely sensed wind vectors over the ocean. *J. Geophys. Res., 87*, 3297-3317, 1982.

Large, W.G., J. Morzel, and G.B. Crawford, Accounting for surface wave distortion of the marine wind profile in low-level ocean storms wind measurements, *J. Phys. Oceanogr., 25*, 2959-2971, 1995.

Long, A. E., C-band V-polarized radar sea-echo model from ERS-

1 Haltenbanken campaign, in *Proceedings of ERS-1 Geophysical Validation, Publ. WPP-36*, edited by M. Wooding, pp. 113-118, Eur. Space Agency, Paris, 1992.

Malardé, J. P., Traitement géométrique et radiométrique du radar diffusiomètre de ERS-1, Thèse de Doctorat, Univ. Paris 7, Paris, 1992.

Petty, G.W., Physical retrievals of over-ocean rain rate from multichannel microwave imagery, 2; Algorithm implementation, *Meteorol. Atmos. Phys., 54*, 101-121, 1994.

Petty, G.W., and K.B. Katsaros, New geophysical algorithms for the special sensor microwave/imager, paper presented at Fifth International Conference on Satellite Meteorology and Oceanography, London, 1990.

Plant, W.J, A two-scale model of short wind-generated waves and scatterometry, *J. Geophys. Res., 91*, 10,735-10,749, 1986.

Quilfen, Y., and A. Bentamy, Calibration/validation of ERS-1 scatterometer precision products, in *Proceedings of IG-ARSS'94*, pp. 945-947, IEEE Press, Piscataway, N.J., 1994.

Quilfen, Y., K.B. Katsaros, and B. Chapron, Structures des champs de vent de surface dans les cyclones tropicaux observés par le diffusiomètre d'ERS-1 et relation avec les vagues et les précipitations, *Mem. Inst. Océanogr., Monaco, 18*, 13-22, 1994.

Stoffelen, A., and D. Anderson, Scatterometer data interpretation: Estimation and validation of the transfer function CMOD4, *J. Geophys. Res., 102*, 5767-5780, 1997.

Tournadre, J., and J.C. Morland, The effect of rain on TOPEX/POSEIDON altimeter data: A new rain flag based on Ku and C band backscatter coefficient, *IEEE Trans. Geosci. Remote Sens.*, in press, 1997.

Witter, D.L., and D.B. Chelton, A Geosat altimeter wind speed algorithm and a method for altimeter wind speed algorithm development, *J. Geophys. Res., 96*, 8853-8860, 1991.

Young I.R., An estimate of the Geosat altimeter wind speed algorithm at high wind speeds, *J. Geophys. Res., 98*, 20,275-20,285, 1993.

B. Chapron, T. Elfouhaily, Y. Quilfen, and J. Tournadre, Laboratoire d'Océanographie Spatiale, IFREMER, BP70, 29280, Plouzané, France. (email: yquilfen@ifremer.fr)

K. Katsaros, Atlantic Oceanographic and Meteorological Laboratory, NOAA, 4301 Rickenbacher Causeway, Miami, FL 33149. (email: katsaros@aoml.noaa.gov)